nature astronomy

ARTICLES

https://doi.org/10.1038/s41550-022-01617-y

Check for updates

Coupling between the accreting corona and the relativistic jet in the microquasar GRS 1915+105

Mariano Méndez[1]✉, Konstantinos Karpouzas[1,2], Federico García[1,3], Liang Zhang[2], Yuexin Zhang[1], Tomaso M. Belloni[4] and Diego Altamirano[2]

Accreting black holes emit highly collimated radio jets expanding at speeds approaching light speed. Some of these jets appear to be expanding at superluminal speeds due to geometric effects. While magnetic fields are thought to be responsible for collimating the ejecta, the mechanism that accelerates the material in these jets remains unexplained. For the galactic black hole GRS 1915+105 with a superluminal radio jet, it has been proposed that thermal instabilities in the accretion disk lead to the ejection of the inner parts of the disk into the jet. Here we use X-ray and radio observations over a 10-year period to reveal a strong correlation between (i) the radio flux that comes from the jet and the flux of the iron emission line that comes from the disk and (ii) the temperature of the hard X-ray corona and the amplitude of a high-frequency variability component that comes from the innermost part of the accretion flow. At the same time, the radio flux and the flux of the iron line are strongly anti-correlated with the temperature of the X-ray corona and the amplitude of the high-frequency variability component. Our findings show that the energy that powers this black hole system can be directed in different proportions either mainly to the X-ray corona or to the jet. These facts, plus our modelling of the variability in this source, suggest that in GRS 1915+105 the X-ray corona turns into the jet.

The X-ray spectrum of black hole binaries can be decomposed into three main radiation components. The first is a thermal component that dominates the emission at low (soft) energies[1], below ~5 keV, due to an accretion disk through which mass flows from the binary companion to the black hole. The second is a power-law like component that dominates the spectrum at energies above ~5–10 keV, caused by inverse Compton scattering of the disk photons in a corona of highly energetic electrons[2]. If the energy distribution of the electrons is Maxwellian, this component features a high-energy cut-off at an energy that depends on the electron temperature of the corona, kT_e. The third is a broad emission line at ~6.5–7 keV due to iron, produced when photons from the corona reflect off the disk, with the line profile being set by special and general relativistic effects[3,4]. The X-ray emission of accreting black hole binaries exhibits high-amplitude variability from tens of milliseconds to decades[5,6]. Depending on the relative importance of these spectral components and the strength of the variability, accreting black holes display different states[7]. In the hard states the X-ray spectrum (~1–20 keV range) is dominated by emission from the corona, and the Fourier power spectrum shows variability of up to 50% of the average luminosity over a broad range of timescales plus narrow quasi-periodic oscillations (QPOs). In the soft states the emission is dominated by the accretion disk, and the variability drops to less than 5% of the average luminosity.

Black hole binaries in the hard states emit in the infrared[8] and radio[9] wavelengths with a spectrum that is consistent with self-absorbed synchrotron radiation from an optically thick and compact jet[10]. During the transition from the hard to the soft states, some black hole binaries show radio emission from individual, spatially resolved, plasma clouds that are ejected in a jet at speeds close to the speed of light. The radio spectrum of these discrete ejections is consistent with synchrotron emission from optically thin material[11].

GRS 1915+105 (ref. [12]) harbours a $12^{+2.0}_{-1.8}$ solar mass black hole[13] and is very variable both in X-rays and radio wavelengths[6,14]. In X-rays, the emission switches from times in which a bright accretion disk with a temperature of $kT_{bb} \approx 2$ keV and a small inner radius dominates the spectrum, to times in which the corona dominates the spectrum, the disk is relatively cool, $kT_{bb} \approx 0.5$–1 keV and the disk is inferred to have a large inner radius[15]. In several observations, mostly those with a cool disk, in addition to a band-limited noise component, a narrow and strong QPO (called type-C QPO[16]) appears in the Fourier power spectrum at frequencies between ~0.4 Hz and 6.5 Hz (ref. [17]). The frequency of the QPO increases as the temperature of the disk increases and the spectrum of the source softens. Besides this QPO (and harmonics and sub-harmonics of the fundamental frequency), the power spectrum of GRS 1915+105 sometimes shows a broad variability component at ~60–80 Hz (ref. [18]) that we will call the high-frequency bump. The high-frequency bump appears when the spectrum of the source is dominated by the corona, but observations in which the corona dominates the emission do not always show this bump. At the same time, observations of GRS 1915+105 in which the spectrum is dominated by the corona are sometimes, but not always, accompanied by high radio fluxes[19,20]. (We show the power density spectra of two observations of GRS 1915+105 with the QPOs and the bump indicated in Supplementary Fig. 1.)

Results

We studied a large dataset of more than 1,800 X-ray observations of GRS 1915+105 obtained with the Rossi X-ray Timing Explorer (RXTE) between 1996 and 2012, combined with almost daily observations of the source at 15 GHz with the Ryle telescope. Our final sample consists of 410 observations for which we have simultaneous X-ray and radio data. For each of these observations we have a

[1]Kapteyn Astronomical Institute, University of Groningen, Groningen, The Netherlands. [2]School of Physics and Astronomy, University of Southampton, Southampton, UK. [3]Instituto Argentino de Radioastronomía, CONICET (CCT La Plata), CICPBA, UNLP, Berazategui, Argentina. [4]Osservatorio Astronomico di Brera, INAF, Merate, Italy. ✉e-mail: mariano@astro.rug.nl

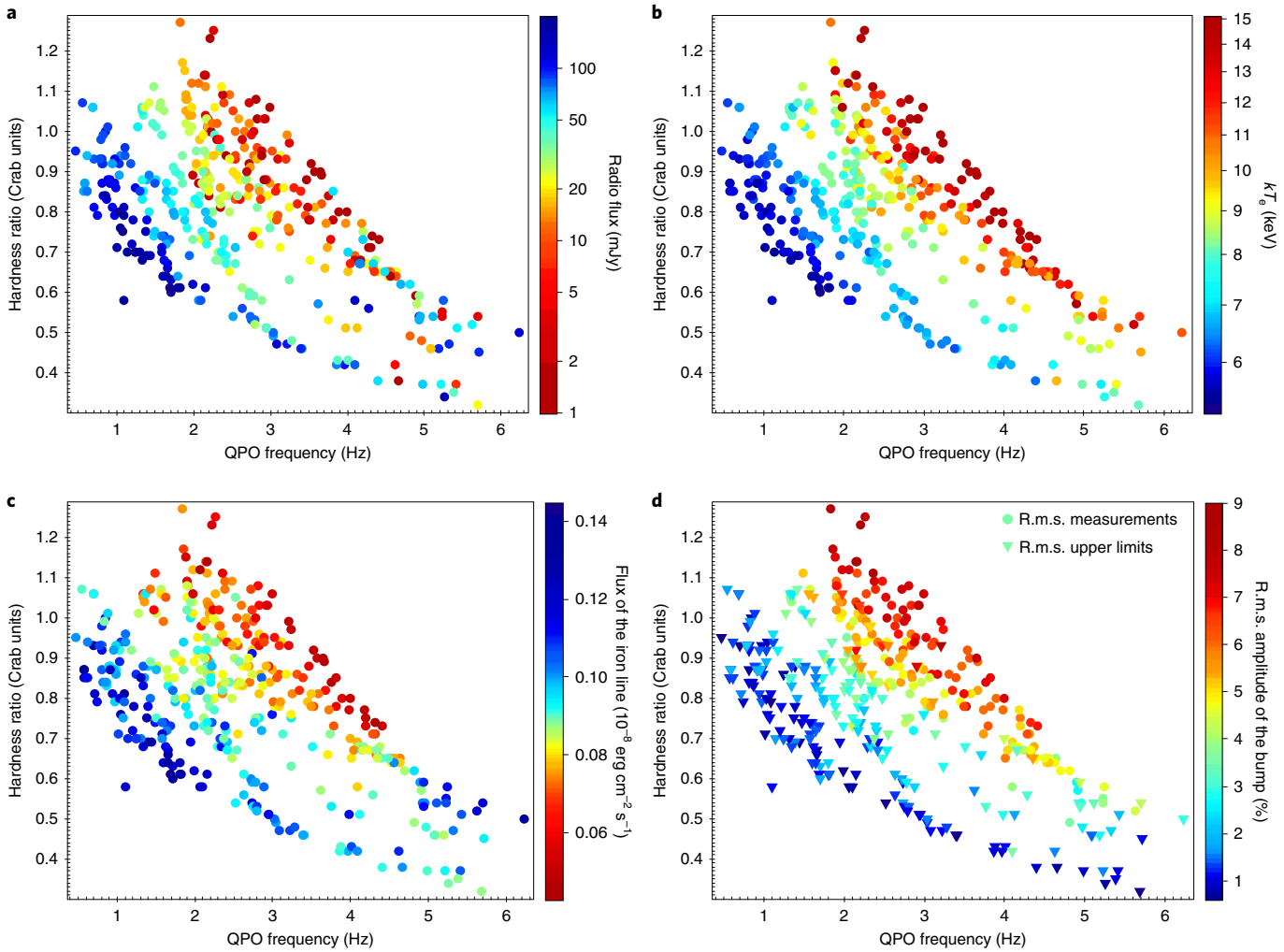

Fig. 1 | Hardness ratio versus QPO frequency of GRS 1915+105. a–d, Each point corresponds to one of the 410 observations of GRS 1915+105. The hardness ratio is the ratio of the observed intensity from 13–60 keV to 2–7 keV in units of the Crab Nebula. Average 1σ errors of the QPO frequency and hardness ratio are $\pm$0.05 Hz and $\pm$0.001 Crab units, respectively, and are both smaller than the size of the points. The colours of the points in each panel represent the 15 GHz radio flux with average 1σ error of $\pm$(1–5) mJy (**a**), the electron temperature of the X-ray corona with 1σ average error of $\pm$0.75 keV (**b**), the flux of the iron emission line with 1σ average error of $\pm 0.7 \times 10^{-10}$ erg cm^{-2} s^{-1} (**c**) and the fractional r.m.s. amplitude of the high-frequency bump with 1σ average error of $\pm$0.7% (**d**). In **d** the circles indicate measured values and the triangles indicate upper limits. (All errors and upper limits in this work represent 1σ and 95% confidence intervals, respectively).

measurement of (i) the radio flux density at 15 GHz, (ii) the X-ray hardness ratio calculated as the ratio of the intensity in the 13–60 keV band to that in the 2–7 keV band, (iii) the frequency of the fundamental component of the type-C QPO, (iv) the phase lag at the QPO frequency for photons in the 5.7–15 keV band with respect to those in the 2–5.7 keV band, (v) the 2–60 keV fractional r.m.s. amplitude of the high-frequency bump and (vi) the best-fitting parameters to the X-ray energy spectra of the source (see Methods for details of the analysis and an explanation of some of these quantities). These vastly different types of data, consisting of X-ray and radio fluxes and spectral and timing properties of a single source, come from wavelengths that are more than eight orders of magnitude apart and sample timescales that are more than eleven orders of magnitude different, from ten milliseconds to a decade.

In Fig. 1 we plot the X-ray hardness ratio as a function of the frequency of the QPO for these 410 observations of GRS 1915+105. The x and y axes of the four panels in this figure are the same, whereas the colours of the points in each panel represent, respectively, the simultaneous 15 GHz radio flux measurements from the jet (Fig. 1a), the electron temperature of the X-ray corona (Fig. 1b), the flux of the iron emission line in the X-ray spectrum (Fig. 1c) and the fractional r.m.s. amplitude of the high-frequency bump (Fig. 1d). The QPO frequency generally increases as the hardness ratio decreases and the source spectrum softens, consistent with a decreasing inner radius of the accretion disk that leads to an increase in both the disk flux[1] and the QPO frequency[21,22]. The relation, however, is strongly broader than the spread expected from the errors in each quantity. (The errors are smaller than the size of the points.)

The colours of the points in the four panels of Fig. 1 show that the radio flux, the flux of the iron line, the temperature of the corona and the fractional r.m.s. amplitude of the high-frequency bump depend upon both QPO frequency and hardness ratio. These four panels show that the breadth of the relation between hardness ratio and QPO frequency is consistently set by the four quantities, such that if we plotted the data in a diagram with the QPO frequency along the x axis, the hardness ratio along the y axis and any of these four quantities along the z axis, the points would lie on a two-dimensional surface in three dimensions.

In Fig. 2 we show the flux of the iron line as a function of the 2–25 keV X-ray flux for all observations of GRS 1915+105. In the

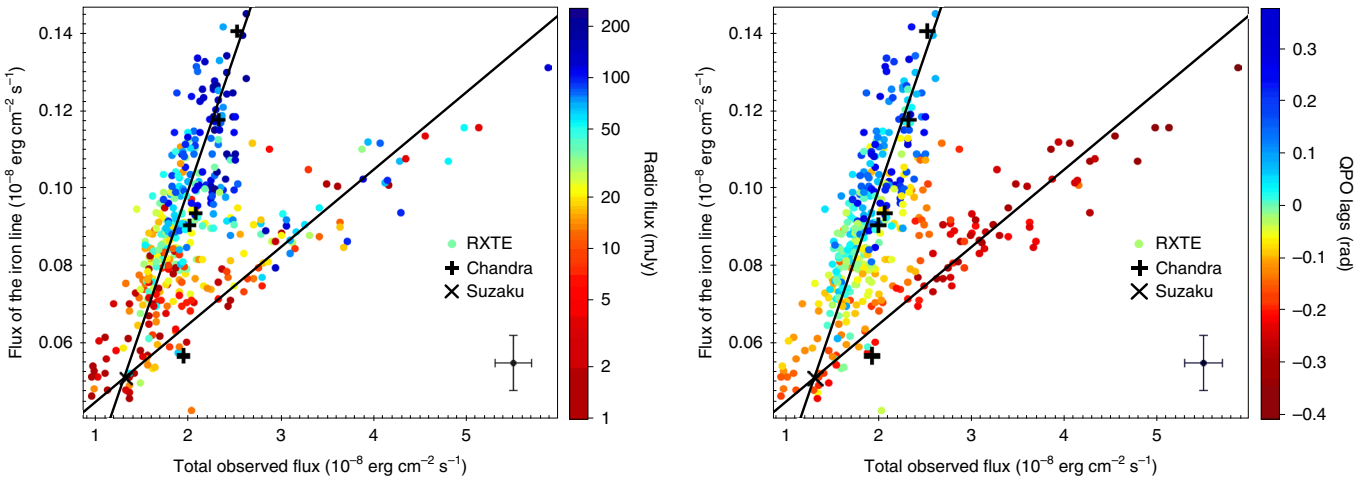

Fig. 2 | Flux of the iron line versus total flux in the 2–25 keV range for GRS 1915+105. Each coloured point corresponds to one of the 410 observations of GRS 1915+105. The colour scale represents the 15 GHz radio flux of the source (left panel) or the phase lags of the QPO in radians (right panel). Negative (positive) lags indicate that, at the QPO frequency, the soft photons in the 2–5.7 keV band arrive after (before) the hard ones in the 5.7–15 keV band. The average 1σ errors of the plotted quantities, $\pm 0.2 \times 10^{-8}$ erg cm^{-2} s^{-1} and $\pm 0.7 \times 10^{-10}$ erg cm^{-2} s^{-1} for the total X-ray flux and the flux of the iron line, respectively, are shown at the bottom right of the plots. The lines indicate the two separate correlations. The plus and cross symbols correspond to measurements of the flux of the line using observations of Chandra[23] and Suzaku[24], respectively.

left panel the colour of the points represents the 15 GHz radio flux of the source, whereas in the right panel the colours represent the phase lags between the 2–5.7 keV and 5.7–15 keV bands at the frequency of the QPO. The flux of the iron line increases as the total flux of the source increases, but when the radio flux is high, the lags at the QPO frequency are positive and the temperature of the corona is low (Fig. 1); the correlation[23] is steeper than when the radio flux is low, the lags are negative and the temperature is high. To confirm that our measurements of the line flux are not biased because of the relatively low spectral resolution of the RXTE Proportional Counter Array (PCA) instrument, we include in this figure independent measurements of the flux of the line with Chandra and Suzaku taken from the literature[23,24] (black plus and cross symbols).

The frequency of the QPO changes in a systematic way along the two correlations in Fig. 2. As the source moves from the top of the flatter correlation to the point where the two correlations cross each other, and then from the bottom to the top of the steeper correlation, the QPO frequency decreases steadily from ~6 Hz to ~0.5 Hz. As the source traces back the same path in the opposite direction, down the steeper and up the flatter correlation, the QPO frequency increases again steadily from ~0.5 Hz to ~6 Hz.

These results provide evidence of a change in the geometry of the corona, and offer a unique clue to understand the nature of the corona and the jet in this object and the nature of the source that powers these components. Inverse Compton scattering cools down the corona by transferring energy from the electrons to the soft disk photons. The temperature of the corona in black hole binaries, however, increases during periods in which the photon flux of the disk drops and Compton cooling is less effective. This means that a source of power balances the inverse Compton cooling and sets the temperature of the corona. Our findings reveal that in GRS 1915+105 the energy provided by this mechanism is split to either power the jet or heat the corona.

The thermal energy stored in a spherical corona of optical depth τ and size L around a black hole of mass M is $E_{\rm th} \approx 3.4 \times 10^{26} \tau \left(\frac{kT_{\rm e}}{1\ {\rm keV}}\right) \left(\frac{M}{M_{\odot}}\right)^2 \left(\frac{L}{R_{\rm g}}\right)^2$ erg, where $M_{\odot}$ is the solar mass, $R_{\rm g} = GM/c^2$ is the gravitational radius of the black hole, and G and c are the gravitational constant and the speed of light, respectively[25]. As discussed in the Supplementary Information, the change of sign of the lags is explained if a fraction of the disk photons that are Comptonized in the corona, which we call the feedback fraction, impinges back onto the disk before reaching the observer[26]. When this feedback fraction (which is between 0 and 1 from its definition) is low, time delays due to Comptonization dominate and the lags are positive; when this fraction is high, reprocessed disk photons reach the observer later than those from the corona and the lags become negative. Taking the corona sizes from fits with this model[27], $L \approx 10$–$1{,}200\, R_{\rm g}$, and $\tau \approx 1$–6 and $kT_{\rm e} \approx 5$–40 keV from the spectral fits, we find that $E_{\rm th} \approx 10^{31}$–$10^{35}$ erg. If this energy is released over the timescale of the high-frequency bump (note that this is the shortest variability timescale in the data; using any other timescale longer than this one to estimate the thermal luminosity would make the discrepancy even bigger), the thermal luminosity is two to five orders of magnitude lower than the observed luminosity of the corona in GRS 1915+105. The alternative is that the corona is powered by magnetic energy[25,28], for example, shear energy due to differential rotation of the magnetic field lines that thread the accretion disk. This magnetic energy would also be responsible for the synchrotron radio emission and the jet ejection mechanism in black hole binaries.

Discussion

Motivated by the above, we propose that in GRS 1915+105 the corona turns into the jet and both are, at different times, the same physical component. The two separate correlations between the iron-line flux and the total flux in Fig. 2 are consistent with the above scenario, and point to a change in the geometry of the corona. When the source is along the flatter correlation, the corona covers the part of the accretion disk that produces the iron line, and the flux line is therefore attenuated[29,30]. When the source is along the steeper correlation, the corona extends vertically, switching to a lamp post geometry[31]; in this phase inverse Compton scattering takes place in the jet, which then illuminates the disk anisotropically[32,33]. Because the jet does not cover the accretion disk, the flux of the iron line is not (or only mildly) attenuated.

Based on the results shown here and based on fits with the model of the lags that we present in the Supplementary Information, the process by which the corona turns into the jet could proceed as follows. First, when the QPO frequency is ~6 Hz the corona is rela-

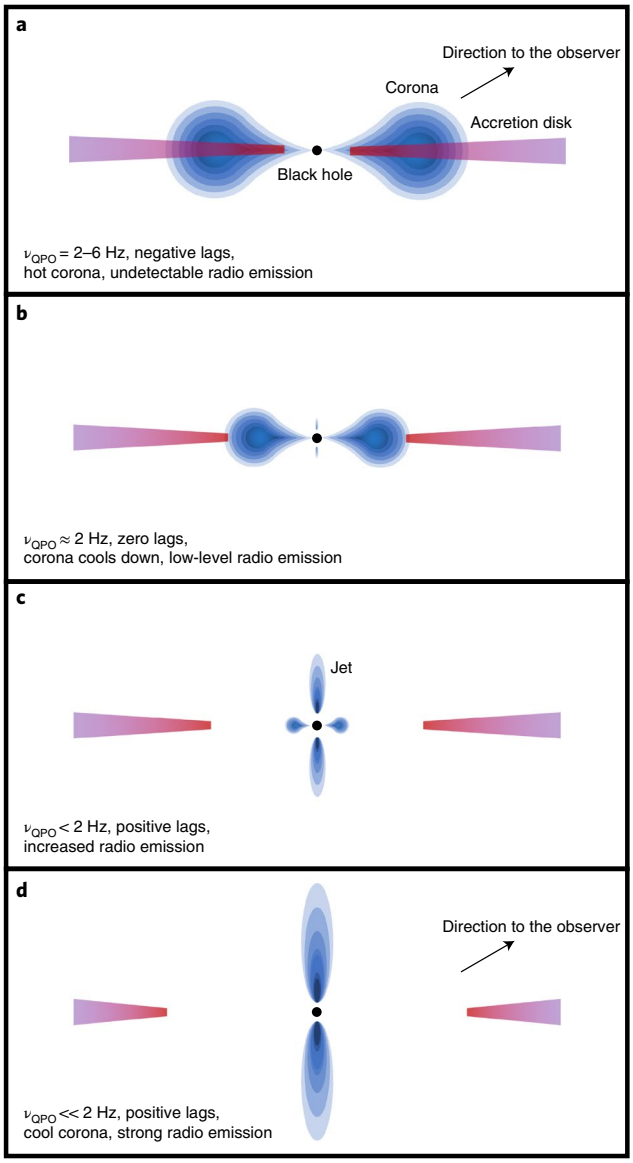

Fig. 3 | Schematic of the corona turning into the jet in GRS 1915+105. a, When the QPO frequency is in the 2–6 Hz range, the lags are negative, the corona is hot and extended, and the corona covers the inner parts of the disk. **b**, The magnitude of the lags and the size of the corona decrease and the inner disk radius increases as the QPO frequency decreases. When the QPO frequency is ~2 Hz, the lags are zero and the size of the corona is equal to the inner radius of the accretion disk. **c**,**d**, As the frequency of the QPO decreases further below ~2 Hz, the lags turn positive and the corona becomes the jet.

tively large and enshrouds the inner parts of the accretion disk (Fig. 3a); as seen from the corona, the disk covers half of the sky and hence there is a high probability that photons from the corona return to the disk, leading to a high feedback fraction and negative QPO lags. As the QPO frequency decreases from ~6 Hz to ~2 Hz, the inner edge of the disk moves outwards and the magnitude of the lags and the size of the corona decrease. In this phase the magnetic field that threads the disk and powers the corona is relatively disorganized, and the magnetic energy is dissipated stochastically, leading to a high corona temperature. Second, at a QPO frequency of ~2 Hz (the transition occurs when the lags of the QPO change from negative to positive; although the exact value of the QPO frequency[17] at which this transition occurs is between 1.8 Hz and 2 Hz, here we will always write 2 Hz for simplicity), the size of the corona becomes equal to the truncation radius of the accretion disk, the feedback fraction decreases abruptly and the QPO lags become zero. From this point on, the corona moves inside the accretion disk (Fig. 3b), the magnetic field starts to become coherent on longer spatial scales, the stochastic energy dissipation decreases and the temperature of the corona drops. At the same time the magnetic field lines start to channel material from the corona into the direction perpendicular to the accretion disk, and low-level radio emission from the jet starts to appear. Third, as the QPO frequency continues decreasing from ~2 Hz to ~0.5 Hz, the inner disk radius moves farther out and the size of the corona increases again but, given that the lags are positive, this time the feedback fraction remains low. From this it follows that the corona does not cover the inner parts of the disk, which can only be the case if the geometry of the corona changes such that it becomes more prominent in the direction perpendicular to the disk (Fig. 3c); as seen from the corona, the disk now covers a much smaller area of the sky. As the magnetic field lines become more spatially coherent[34], there is less stochastic energy dissipation, the corona temperature drops further, and the material from the corona that was channelled off the originally extended corona is expelled away from the accretion-disk plane and becomes the radio jet (Fig. 3d).

Our multi-wavelength correlations match the proposal that, during the initial parts of an outburst, the X-ray corona of the black hole binary MAXI J1820+070 contracts[35] and then re-expands[36]. Here we show that, as previously speculated[37–39], in the case of GRS 1915+105 the contracting corona becomes the radio jet and that, at least part of the time, the corona and the jet are actually one and the same physical component[40–42].

The appearance of radio flares when the QPO frequency is below 2 Hz reinforces our interpretation. Figure 4 shows that in the periods in which the frequency of the QPO moves more or less stochastically between ~2 Hz and ~8 Hz (red circles), the radio flux (light blue curve) is low. Occasionally, the QPO frequency evolves in a more systematic way: it starts to decrease and crosses below the value of 2 Hz (blue-red points), and at the same time the radio flux increases sharply and a radio flare lasting a few tens of days is observed. Figure 4 shows this behaviour over a period of about 500 days in which the source shows two radio flares. Supplementary Fig. 5 shows that the same behaviour repeats consistently over a period of 10 years and about a dozen radio flares.

The behaviour we observe in GRS 1915+105 could explain the deviations from a single track in the radio and X-ray correlation of other accreting galactic black holes[43–48]. In Supplementary Fig. 7 we show that in the observations of GRS 1915+105 presented here the radio and X-ray flux are strongly correlated when the corona temperature is low and the lags of the QPO are positive, but they are uncorrelated when the corona temperature is high and the lags of the QPO are negative. If, as in the case of GRS 1915+105, the energy powering these systems is used to either accelerate the jet or heat the corona, different sources, or the same source at different times, will show lower radio fluxes at a given X-ray flux (or, equivalently, higher X-ray fluxes at a given radio flux), depending on how much energy is directed towards launching the radio jet or heating the X-ray corona, respectively. In principle, the same channelling of energy to the jet and the corona should happen in supermassive black holes, and should therefore apply to the full range of black hole masses in the fundamental plane of black hole activity[49]. Interestingly, it has been recently shown that radio-loud and radio-quiet quasars trace two separate planes in a plot of radio luminosity versus X-ray luminosity and black hole mass[50]. We speculate that, as in the case of GRS 1915+105 (Supplementary Fig. 7), these two relations reflect the fact that the temperature of the corona is higher in radio-quiet quasars than in radio-loud quasars.

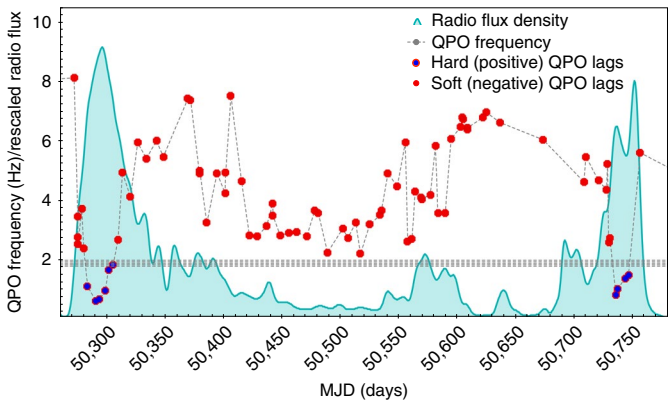

Fig. 4 | Time evolution of QPO frequency and radio flux for GRS 1915+105. The points connected by a line show the time evolution of the frequency of the QPO in the X-ray power spectrum of GRS 1915+105. (The 1σ error of the QPO frequency is ±0.05 Hz.) The light blue curve (smoothed with a Gaussian kernel) shows the simultaneous measurements of the radio flux density at 15 GHz with the y axis rescaled. (The 1σ error of the radio flux is ±(1–5) mJy.) A strong radio flare appears on the two occasions in which the lags of the QPO turn from soft (red points) to hard (blue-red points), corresponding to the QPO frequency crossing from above to below ~2 Hz. The horizontal band shows the range of QPO frequencies over which the transition occurs. Here we show the first two radio flares in our data, but the same behaviour occurs consistently for all radio flares during our observations (Supplementary Information). MJD, modified Julian date.

Methods

Power spectra. We examined all the RXTE archival observations of GRS 1915+105 from 1996 to 2012 obtained with the PCA. The observations that we used for our analysis belong to the class χ (ref. [6]), state C, equivalent to one of the hard states in other (transient) black hole sources. For each observation we computed the Fourier power spectrum in the full energy band (absolute PCA channel 0–249) every 128 s with a time resolution of 1/512 s, corresponding to a Nyquist frequency of 256 Hz. We averaged all the 128 s power spectra within an observation, subtracted the contribution due to Poisson noise[51] and normalized[52] these averaged power spectra to units of fractional r.m.s. squared per hertz. (We ignored the background count rate for this calculation as it was always negligible compared to the source count rate.) We subsequently applied a logarithmic frequency re-bin to the data such that the size of a bin increases by exp(1/100) with respect to the size of the previous one, and we used XSPEC version 12.9 to fit the resulting power spectra with a sum of Lorentzian functions[53] that represent the broadband noise component and a number of QPOs[17]. As in previous studies[18] we included a Gaussian component centred at zero frequency in the model to fit a high-frequency bump at 60–80 Hz in the power spectra. (We show two power spectra with the best-fitting model in Supplementary Fig. 1.) For the rest of the analysis we selected only observations in which at least one narrow QPO peak is present on top of the broadband noise component in the power spectra, which is typical for the type-C QPOs[16]. Based on the fitting results we retained only features that were detected at a significance greater than 3σ and had a Q factor, defined as the ratio of the QPO frequency to its width, of 2 or more. We further checked the spectrogram of each observation, which shows visually the Fourier power spectrum as it varies with time, and excluded ~130 observations in which the QPO frequency changed strongly within a full RXTE observation. Our final sample contains a total of 620 observations.

Lag spectra. Following the method described in refs. [54,55], we produced a frequency-dependent phase-lag spectrum (lag–frequency spectrum) between the 2–5.7 and 5.7–15 keV energy bands for each observation. As our sample includes observations during the PCA calibration epochs 3–5, to account for changes in the PCA channel-to-energy gain factor we selected the closest absolute channels that matched these energy bands, but the exact boundaries of each band still differ slightly between epochs. To calculate the phase lags of the QPO, we averaged the lag–frequency spectra around the centroid frequency of the QPO, $\nu_0 \pm$FWHM/2, where FWHM is the full width at half maximum of the Lorentzian that we used to fit the QPO profile. In principle, the phase lags in the range of frequencies of the QPO can be affected by the lags of the underlying broadband noise component. However, in GRS 1915+105 the r.m.s. amplitude of the QPO is much higher than that of the broadband noise and the phase lags at the frequency of the QPO are dominated by the QPO itself, with the contribution of the noise component being negligible[56]. In this work, a positive (negative) lag means that the hard photons lag (lead) the soft photons. No correction for the dead-time-driven crosstalk[57] was done because this effect was found to be negligible. (See ref. [17] for other details of the timing analysis.) In Supplementary Fig. 2 we show nine representative power and lag–frequency spectra covering the range of frequencies of the QPO in GRS 1915+105.

Energy spectra. We used the RXTE PCA Standard 2 data to extract energy spectra separately for each observation in our sample. (We also fitted the RXTE High Energy X-ray Timing Experiment (HEXTE) data of those observations in which the instrument was operational; the results were consistent with those of the RXTE PCA, but as data of this instrument were not available for all observations, we did not use the RXTE HEXTE data for the rest of the analysis.) We corrected the energy spectra for dead time and used the FTOOLS PCABACKEST and PCARSP in HEADAS version 6.27 to, respectively, extract background spectra and produce response files for each observation. We fitted the energy spectra of all observations jointly with the model VPHABS*(DISKBB+GAUSS+NTHCOMP). The component VPHABS accounts for the interstellar absorption along the line of sight to the source; we used the abundance and cross-section tables given by ref. [58] and ref. [59], respectively, with the column density of hydrogen, $N_{\rm H}$, linked across observations and free to vary. Because $N_{\rm H}$ in the direction of GRS 1915+105 is quite high[60] ($N_{\rm H} \gtrsim 6 \times 10^{22}$ atoms cm^{-2}), we also made the abundance of iron in the interstellar material free to vary, as neutral iron produces an absorption edge at $E \approx 7.1$ keV that was apparent in the fit residuals. The component DISKBB[61] represents the emission from an optically thick and geometrically thin accretion disk, and has parameters $kT_{\rm bb}$ and $N_{\rm dbb}$ that are, respectively, the temperature at the inner disk radius and the normalization of the component defined as the ratio of the inner disk radius to the distance to the source squared multiplied by the cosine of the inclination of the disk with respect to the line of sight. The component NTHCOMP[62] represents the emission due to inverse Compton scattering from the corona. The parameters of this component are the power-law index, Γ; the electron temperature of the corona, $kT_{\rm e}$; the temperature of the source of soft photons that enter into, and are upscattered in, the corona, $kT_{\rm seed}$; and a normalization that gives the flux density at 1 keV. We assumed that the source of seed soft photons is the accretion disk, and linked the temperature $kT_{\rm seed}$ to the temperature of the DISKBB component for each observation separately during the fits. In this model, the optical depth of the corona, τ, assumed to be homogeneous, is a function[2] of Γ and $kT_{\rm e}$. Finally, the component GAUSS represents a broad iron emission line at 6.5–7 keV due to reflection of corona photons off the accretion disk[3,4]. Although a full reflection model[63,64] would be more appropriate to describe this effect, the PCA instrument does not have enough spectral resolution to distinguish between the profile of a line in a full reflection model and a Gaussian component. The parameters of the GAUSS component are the energy, width and total photon flux of the line, or $E_{\rm g}$, σ and $N_{\rm g}$, respectively. Finally, we calculated the total observed flux of the source and the intrinsic (that is, not affected by interstellar absorption) flux of the full model and of all the individual model components in the 2–25 keV energy range. In Supplementary Fig. 3 we show the energy spectra, with the best-fitting model, of the same two observations in Supplementary Fig. 1.

If the iron emission line is due to reflection of corona photons off the accretion disk, and the width of the line is a consequence of Doppler boosting, Doppler beaming and gravitational redshift, it would be more appropriate to use a full reflection component that includes relativistic broadening instead of a Gaussian to fit the spectrum. To explore this we fitted all the spectra with the model VPH ABS*(DISKBB+RELXILLCP+NTHCOMP), where the component REXILLCP[64] represents the reflection off the accretion disk of the emission from the NTHCOMP component. Compared to the fits with a Gaussian, this model has six extra free parameters. Given that the RXTE PCA instrument has limited spectral resolution and does not extend below ~3 keV, the model is insensitive to some of the parameters of REXILLCP, and some of these parameters become highly correlated with those of the DISKBB component. We therefore fixed the spin of the black hole to $a_* = 0.95$ (ref. [60]) and the inclination angle of the accretion disk to the line of sight to $i = 65°$ (ref. [11]). We further linked the two emissivity indices during the fits, which eliminates the parameter that gives the radius in the disk at which the power-law index of the emissivity profile changes, and fixed the inner radius of the disk at the radius of the innermost stable circular orbit[60]. Finally, we linked the power-law index, Γ, and the electron temperature, $kT_{\rm e}$, of RELXILLCP to the corresponding parameters of NTHCOMP. The extra free parameters of the fit are one emissivity index, the reflection fraction, the ionization parameter and the iron abundance of the disk. We obtain fits as good as those of the previous model, with the reflection fraction ranging from 1% to 20%. As the reflected component is much lower than the Comptonized component, the parameters of the NTHCOMP in these fits are consistent with those from the fits with a Gaussian line. The biggest impact of fitting the spectra with a reflection component is that the parameters of the disk are less well constrained in the model with REXILLCP than in the model with a Gaussian. This is understandable given that the emission of the reflection component at energies below ~4–5 keV, where the disk emission peaks, is higher than that of a Gaussian.

The REXILLCP model does not provide the flux or the equivalent width of the Gaussian; however, the reflection fraction of REXILLCP is generally correlated

with the parameters of the line[65]. We plotted the flux of the iron line from the fits with a Gaussian against the reflection fraction from the fits with REXILLCP and confirmed that this is indeed the case in our fits. We therefore obtain plots similar to those in Fig. 2 if instead of the flux of the Gaussian line we plot the reflection fraction of REXILLCP versus total flux. We prefer to use the former because, as we explained above, the model with a Gaussian line has fewer free parameters than the full reflection model, which, given the limited spectral resolution of the RXTE PCA instrument, leads to degeneracies of the parameters in the fits with the full reflection model, and because by using a Gaussian we can easily include in the plot the measurements of the flux of the iron line obtained with Chandra and Suzaku, as we did in Fig. 2.

Hardness ratio. For each RXTE observation of GRS 1915+105 we computed a hardness ratio value defined as the ratio of the background-subtracted count rate of the source in the 13–60 keV band to that in the 2–7 keV band. As with the lag–frequency spectra, we selected the closest absolute channels that matched these energy bands in each PCA gain epoch. Before calculating the ratios, we corrected each observed count rate for instrumental dead time and normalized it by the count rate in the same band from the Crab Nebula to account for possible changes of the effective area of the instrument with time.

Radio fluxes. For the flux density data of GRS 1915+105 in radio, we used measurements[14] from the Ryle Telescope at 15 GHz with the four mobile antennas set in a compact array configuration within 100 m of the nearest fixed antenna, yielding a resolution of ~30 arcsec at that frequency. The flux density scale was calibrated with observations of the nearby quasars 3C 48 or 3C 286. The observations consist mostly of 32 s samples with an r.m.s. noise of 6 mJy that decreases as the square root of the integration time; flux density values below about 1 mJy may be unreliable. See ref. [14] for other details of the analysis of the radio data.

Finally, we cross-correlated all the X-ray and radio data based on the date of the observations, which left us with a sample of 410 observations with simultaneous radio flux densities at 15 GHz and X-ray energy, power density and lag–frequency spectra, and hardness ratios.

Having described the observations and analysis we used, we note that the measurements presented in this paper come from very different types of data and totally independent analysis techniques. The hardness ratio, iron-line flux and kT_e come from X-ray light curves and time-averaged energy spectra. The frequency and lags of the QPO and the r.m.s. amplitude of the high-frequency bump come from Fourier power spectra of high-time-resolution data. The radio flux was measured independently in a frequency band totally different from that of the X-ray data.

Data availability

All the X-ray data used in this study are available from NASA's High Energy Astrophysics Science Archive Research Center (https://heasarc.gsfc.nasa.gov/). The radio data used in this study are available at http://www.astro.rug.nl/~mariano/GRS_1915+105_Ryle_data_1995-2006.txt.

Code availability

The data reduction was done using HEADAS version 6.27, whereas the model fitting of energy, power and lag–energy spectra was done with XSPEC; both packages are available at the HEASARC website (https://heasarc.gsfc.nasa.gov/). The timing analysis was performed with the GHATS package developed by T.M.B. and is available upon request (http://astrosat.iucaa.in/~astrosat/GHATS_Package/Home.html). All figures were made in TOPCAT, a JAVA-based scientific plotting package developed by M. Taylor (http://www.star.bris.ac.uk/~mbt/topcat/).

Received: 2 October 2021; Accepted: 27 January 2022;
Published online: 7 March 2022

References

1. Shakura, N. I. & Sunyaev, R. A. Black holes in binary systems. Observational appearance. *Astron. Astrophys.* **24**, 337–355 (1973).
2. Sunyaev, R. A. & Titarchuk, L. G. Comptonization of X-rays in plasma clouds. Typical radiation spectra. *Astron. Astrophys.* **86**, 121–138 (1980).
3. Fabian, A. C., Rees, M. J., Stella, L. & White, N. E. X-ray fluorescence from the inner disc in Cygnus X-1. *Mon. Not. R. Astron. Soc.* **238**, 729–736 (1989).
4. Fabian, A. C. et al. Broad line emission from iron K- and L-shell transitions in the active galaxy 1H 0707-495. *Nature* **459**, 540–542 (2009).
5. Greiner, J., Morgan, E. H. & Remillard, R. A. Rossi X-Ray Timing Explorer observations of GRS 1915+105. *Astrophys. J. Lett.* **473**, L107 (1996).
6. Belloni, T., Klein-Wolt, M., Méndez, M., van der Klis, M. & van Paradijs, J. A model-independent analysis of the variability of GRS 1915+105. *Astron. Astrophys.* **355**, 271–290 (2000).
7. Méndez, M. & van der Klis, M. The EXOSAT data on GX 339-4: further evidence for an 'intermediate' state. *Astrophys. J.* **479**, 926–932 (1997).
8. Eikenberry, S. S., Matthews, K., Morgan, E. H., Remillard, R. A. & Nelson, R. W. Evidence for a disk-jet interaction in the microquasar GRS 1915+105. *Astrophys. J. Lett.* **494**, L61–L64 (1998).
9. Mirabel, I. F. et al. Accretion instabilities and jet formation in GRS 1915+105. *Astron. Astrophys.* **330**, L9–L12 (1998).
10. Fender, R. P., Spencer, R. E., Newell, S. J. & Tzioumis, A. K. High-resolution radio observations of the black hole candidate GX 339-4. *Mon. Not. R. Astron. Soc.* **286**, L29–L32 (1997).
11. Mirabel, I. F. & Rodríguez, L. F. A superluminal source in the Galaxy. *Nature* **371**, 46–48 (1994).
12. Fender, R. & Belloni, T. GRS 1915+105 and the disc-jet coupling in accreting black hole systems. *Annu. Rev. Astron. Astrophys.* **42**, 317–364 (2004).
13. Reid, M. J. et al. A parallax distance to the microquasar GRS 1915+105 and a revised estimate of its black hole mass. *Astrophys. J.* **796**, 2 (2014).
14. Pooley, G. G. & Fender, R. P. The variable radio emission from GRS 1915+105. *Mon. Not. R. Astron. Soc.* **292**, 925–933 (1997).
15. Belloni, T., Méndez, M., King, A. R., van der Klis, M. & van Paradijs, J. A unified model for the spectral variability in GRS 1915+105. *Astrophys. J. Lett.* **488**, L109–L112 (1997).
16. Casella, P., Belloni, T. & Stella, L. The ABC of low-frequency quasi-periodic oscillations in black hole candidates: analogies with Z sources. *Astrophys. J.* **629**, 403–407 (2005).
17. Zhang, L. et al. A systematic analysis of the phase lags associated with the type-C quasi-periodic oscillation in GRS 1915+105. *Mon. Not. R. Astron. Soc.* **494**, 1375–1386 (2020).
18. Trudolyubov, S. P. On the two types of steady hard X-ray states of GRS 1915+105. *Astrophys. J.* **558**, 276–282 (2001).
19. Muno, M. P., Morgan, E. H. & Remillard, R. A. Quasi-periodic oscillations and spectral states in GRS 1915+105. *Astrophys. J.* **527**, 321–340 (1999).
20. Fender, R. P. et al. MERLIN observations of relativistic ejections from GRS 1915+105. *Mon. Not. R. Astron. Soc.* **304**, 865–876 (1999).
21. Stella, L. & Vietri, M. Lense-Thirring precession and quasi-periodic cscillations in low-mass X-ray binaries. *Astrophys. J. Lett.* **492**, L59–L62 (1998).
22. Ingram, A., Done, C. & Fragile, P. C. Low-frequency quasi-periodic oscillations spectra and Lense-Thirring precession. *Mon. Not. R. Astron. Soc.* **397**, L101–L105 (2009).
23. Neilsen, J. & Lee, J. C. Accretion disk winds as the jet suppression mechanism in the microquasar GRS 1915+105. *Nature* **458**, 481–484 (2009).
24. Mizumoto, M., Ebisawa, K., Tsujimoto, M. & Inoue, H. Origin of the X-ray broad iron spectral feature in GRS 1915+105. *Publ. Astron. Soc. Jpn* **68**, S16 (2016).
25. Merloni, A. & Fabian, A. C. Accretion disc coronae as magnetic reservoirs. *Mon. Not. R. Astron. Soc.* **321**, 549–552 (2001).
26. Karpouzas, K. et al. The Comptonizing medium of the neutron star in 4U 1636 − 53 through its lower kilohertz quasi-periodic oscillations. *Mon. Not. R. Astron. Soc.* **492**, 1399–1415 (2020).
27. Karpouzas, K. et al. A variable corona for GRS 1915+105. *Mon. Not. R. Astron. Soc.* **503**, 5522–5533 (2021).
28. Malzac, J., Merloni, A. & Fabian, A. C. Jet–disc coupling through a common energy reservoir in the black hole XTE J1118+480. *Mon. Not. R. Astron. Soc.* **351**, 253–264 (2004).
29. Matt, G., Fabian, A. C. & Reynolds, C. S. Geometrical and chemical dependence of K-shell X-ray features. *Mon. Not. R. Astron. Soc.* **289**, 175–184 (1997).
30. Petrucci, P. O., Merloni, A., Fabian, A., Haardt, F. & Gallo, E. The effects of a Comptonizing corona on the appearance of the reflection components in accreting black hole spectra. *Mon. Not. R. Astron. Soc.* **328**, 501–510 (2001).
31. Miniutti, G. & Fabian, A. C. A light bending model for the X-ray temporal and spectral properties of accreting black holes. *Mon. Not. R. Astron. Soc.* **349**, 1435–1448 (2004).
32. Kylafis, N. D., Reig, P. & Papadakis, I. A quantitative explanation of the type-B QPOs in GX 339-4. *Astron. Astrophys.* **640**, L16 (2020).
33. Reig, P. & Kylafis, N. D. Illumination of the accretion disk in black hole binaries: an extended jet as the primary source of hard X-rays. *Astron. Astrophys.* **646**, A112 (2021).
34. Meier, D. L. Magnetically dominated accretion flows (MDAFS) and jet production in the lowhard state. *Astrophys. Space Sci.* **300**, 55–65 (2005).
35. Kara, E. et al. The corona contracts in a black-hole transient. *Nature* **565**, 198–201 (2019).
36. Wang, J. et al. Disk, corona, jet connection in the intermediate state of MAXI J1820+070 revealed by NICER spectral-timing analysis. *Astrophys. J. Lett.* **910**, L3 (2021).
37. Vadawale, S. V. et al. On the origin of the various types of radio emission in GRS 1915+105. *Astrophys. J.* **597**, 1023–1035 (2003).
38. Rodriguez, J., Corbel, S. & Tomsick, J. A. Spectral evolution of the microquasar XTE J1550−564 over its entire 2000 outburst. *Astrophys. J.* **595**, 1032–1038 (2003).

39. Fender, R. P., Belloni, T. M. & Gallo, E. Towards a unified model for black hole X-ray binary jets. *Mon. Not. R. Astron. Soc.* **355**, 1105–1118 (2004).
40. Levinson, A. & Blandford, R. On the jets associated with Galactic superluminal sources. *Astrophys. J. Lett.* **456**, L29–L32 (1996).
41. Giannios, D., Kylafis, N. D. & Psaltis, D. Spectra and time variability of Galactic black-hole X-ray sources in the low/hard state. *Astron. Astrophys.* **425**, 163–169 (2004).
42. Markoff, S., Nowak, M. A. & Wilms, J. Going with the flow: can the base of jets subsume the role of compact accretion disk coronae? *Astrophys. J.* **635**, 1203–1216 (2005).
43. Hannikainen, D. C., Hunstead, R. W., Campbell-Wilson, D. & Sood, R. K. MOST radio monitoring of GX 339−4. *Astron. Astrophys.* **337**, 460–464 (1998).
44. Corbel, S., Nowak, M. A., Fender, R. P., Tzioumis, A. K. & Markoff, S. Radio/X-ray correlation in the low/hard state of GX 339−4. *Astron. Astrophys.* **400**, 1007–1012 (2003).
45. Gallo, E., Fender, R. P. & Pooley, G. G. A universal radio–X-ray correlation in low/hard state black hole binaries. *Mon. Not. R. Astron. Soc.* **344**, 60–72 (2003).
46. Coriat, M. et al. Radiatively efficient accreting black holes in the hard state: the case study of H1743−322. *Mon. Not. R. Astron. Soc.* **414**, 677–690 (2011).
47. Gallo, E., Miller, B. P. & Fender, R. Assessing luminosity correlations via cluster analysis: evidence for dual tracks in the radio/X-ray domain of black hole X-ray binaries. *Mon. Not. R. Astron. Soc.* **423**, 590–599 (2012).
48. Gallo, E., Degenaar, N. & van den Eijnden, J. Hard state neutron star and black hole X-ray binaries in the radio:X-ray luminosity plane. *Mon. Not. R. Astron. Soc.* **478**, L132–L136 (2018).
49. Merloni, A., Heinz, S. & di Matteo, T. A Fundamental Plane of black hole activity. *Mon. Not. R. Astron. Soc.* **345**, 1057–1076 (2003).
50. Bariuan, L. G. C., Snios, B., Sobolewska, M., Siemiginowska, A. & Schwartz, D. A. The fundamental planes of black hole activity for radio-loud and radio-quiet quasars. Preprint at https://arxiv.org/abs/2201.04666 (2022).
51. Zhang, W., Jahoda, K., Swank, J. H., Morgan, E. H. & Giles, A. B. Dead-time modifications to fast Fourier transform power spectra. *Astrophys. J.* **449**, 930–935 (1995).
52. Belloni, T. & Hasinger, G. An atlas of aperiodic variability in HMXB. *Astron. Astrophys.* **230**, 103–119 (1990).
53. Nowak, M. A. Are there three peaks in the power spectra of GX 339-4 and Cyg X-1? *Mon. Not. R. Astron. Soc.* **318**, 361–367 (2000).
54. Vaughan, B. A. & Nowak, M. A. X-ray variability coherence: how to compute it, what it means, and how it constrains models of GX 339−4 and Cygnus X-1. *Astrophys. J. Lett.* **474**, L43–L46 (1997).
55. Nowak, M. A., Vaughan, B. A., Wilms, J., Dove, J. B. & Begelman, M. C. Rossi X-Ray Timing Explorer observation of Cygnus X-1. II. Timing analysis. *Astrophys. J.* **510**, 874–891 (1999).
56. van den Eijnden, J., Ingram, A. & Uttley, P. Probing the origin of quasi-periodic oscillations: the short-time-scale evolution of phase lags in GRS 1915+105. *Mon. Not. R. Astron. Soc.* **458**, 3655–3666 (2016).
57. van der Klis, M. et al. The complex cross-spectra of Cygnus X-2 and GX 5-1. *Astrophys. J. Lett.* **319**, L13 (1987).
58. Wilms, J., Allen, A. & McCray, R. On the absorption of X-rays in the interstellar medium. *Astrophys. J.* **542**, 914–924 (2000).
59. Verner, D. A., Ferland, G. J., Korista, K. T. & Yakovlev, D. G. Atomic data for astrophysics. II. New analytic FITS for photoionization cross sections of atoms and ions. *Astrophys. J.* **465**, 487–498 (1996).
60. Miller, J. M. et al. NuSTAR spectroscopy of GRS 1915+105: disk reflection, spin, and connections to jets. *Astrophys. J. Lett.* **775**, L45 (2013).
61. Mitsuda, K. et al. Energy spectra of low-mass binary X-ray sources observed from Tenma. *Publ. Astron. Soc. Jpn* **36**, 741–759 (1984).
62. Zdziarski, A. A., Johnson, W. N. & Magdziarz, P. Broad-band γ-ray and X-ray spectra of NGC 4151 and their implications for physical processes and geometry. *Mon. Not. R. Astron. Soc.* **283**, 193–206 (1996).
63. García, J. et al. Improved reflection models of black hole accretion disks: treating the angular distribution of X-rays. *Astrophys. J.* **782**, 76 (2014).
64. Dauser, T., García, J., Parker, M. L., Fabian, A. C. & Wilms, J. The role of the reflection fraction in constraining black hole spin. *Mon. Not. R. Astron. Soc.* **444**, L100–L104 (2014).
65. Dunn, R. J. H., Fender, R. P., Körding, E. G., Cabanac, C. & Belloni, T. Studying the X-ray hysteresis in GX 339-4: the disc and iron line over one decade. *Mon. Not. R. Astron. Soc.* **387**, 545–563 (2008).

Acknowledgements

This work is part of the research programme Athena with project number 184.034.002, which is (partly) financed by the Dutch Research Council (NWO). F.G. is a researcher of CONICET, and acknowledges support by PIP 0113 (CONICET) and PICT-2017-2865 (ANPCyT). Y.Z. acknowledges support from a China Scholarship Council scholarship (201906100030). T.M.B. acknowledges financial contribution from agreement ASI-INAF n.2017-14-H.0 and from PRIN-INAF 2019 N.15, and thanks the Team Meeting at the International Space Science Institute (Bern) for fruitful discussions. D.A. acknowledges support from the Royal Society. We thank G. Pooley for making the radio data available. This research has made use of data and/or software provided by the High Energy Astrophysics Science Archive Research Center (HEASARC), which is a service of the Astrophysics Science Division at NASA/GSFC. This research made use of NASA's Astrophysics Data System. We thank O. Blaes for discussions and ideas that helped us improve this manuscript.

Author contributions

All authors contributed to interpretation of results and edited the manuscript. M.M. led the interpretation, obtained spectral parameters and wrote the manuscript. K.K. wrote the model that triggered this research, produced initial radio and timing plots, fitted r.m.s. and lag spectra and co-led the interpretation. F.G. produced initial three-dimensional radio, timing and spectral plots, fitted r.m.s. and lag spectra of the QPO and co-led the interpretation. M.M., K.K. and F.G. measured extra QPO frequencies. L.Z. obtained parameters of the QPO. Y.Z. obtained parameters of the high-frequency bump. T.M.B. had the idea to study the high-frequency bump in connection with the radio flux. D.A. discussed the results and contributed to the interpretation.

Competing interests

The authors declare no competing interests.

Additional information

Supplementary information The online version contains supplementary material available at https://doi.org/10.1038/s41550-022-01617-y.

Correspondence and requests for materials should be addressed to Mariano Méndez.

Peer review information *Nature Astronomy* thanks the anonymous reviewers for their contribution to the peer review of this work.

Reprints and permissions information is available at www.nature.com/reprints.

Publisher's note Springer Nature remains neutral with regard to jurisdictional claims in published maps and institutional affiliations.